

# SUITABILITY OF IMMERSED-BOUNDARY METHODS FOR HIGH-FIDELITY COMPUTATIONAL AEROACOUSTICS

*A. Lázaro<sup>1,2</sup>, S. Madriñan<sup>2</sup>, O. Carrasco<sup>2</sup>, J. Grau<sup>1</sup>,  
R. Torres<sup>1</sup>, L. Jofre<sup>1</sup> and F. Capuano<sup>1</sup>*

<sup>1</sup> *Department of Fluid Mechanics, Universitat Politècnica de Catalunya · BarcelonaTech*  
<sup>2</sup> *QEV Technologies S.L.*

*francesco.capuano@upc.edu*

## Abstract

This work presents a preliminary assessment of the suitability of the immersed boundary method (IBM) for high-fidelity direct sound computations. A ghost-cell IBM is implemented in conjunction with a recently developed non-dissipative and robust numerical framework based on kinetic-energy and pressure-equilibrium preserving discretizations. The strategy is validated using the well-known canonical benchmark of acoustic scattering of a steady cylinder, providing accurate results and thus holding great promise for its application in complex scenarios.

## 1 Introduction

The computational fluid dynamics (CFD) community is leading a transition from traditional lower-fidelity strategies to embracing high-fidelity scale-resolving simulations for the solution of complex industrial flows. One of the main challenges towards this goal is to be able to combine accurate numerical schemes with complex geometries at an affordable cost. In this regard, the field of computational aeroacoustics (CAA) is a major example where implementing this paradigm shift is especially complex. The direct computation of sound generation/propagation through fully-resolved numerical simulations of the compressible Navier-Stokes equations requires high-order non-dissipative and non-dispersive discrete operators, which are difficult to implement in the context of unstructured or even body-conforming meshes, as discussed by Colonius and Lele (2004). Consequently, the vast majority of aeroacoustic studies have typically relied on lower-fidelity cost-effective approaches, such as acoustic analogies or splitting methods. In this work, it is conjectured that a proper combination of: i) an immersed boundary method (IBM) and ii) a physics-compatible discretization framework can pave the way for high-fidelity direct sound computations.

The IBM is a broad class of numerical algorithms where the governing equations are solved on a non-conforming regular Cartesian mesh, and the presence of a body is accounted for through suitable forcing schemes, implemented either within the continuous model or directly at the discrete level – see e.g., the recent review by Verzicco (2023) for a historical ac-

count of IBMs. Despite the fact that the IBM was initially conceived for compressible flows, its development and application for wave-dominated problems, and specifically for CAA, has been quite limited. For instance, Seo & Mittal (2011) proposed a high-order IBM to solve the linearized perturbation equations in the context of an acoustic splitting methodology. Their method needed a spatial filter to ensure numerical stability. More recently, Wang et al. (2020) coupled the IBM with a high-order upwind-biased scheme (T/WENO) for direct sound computations.

Here, the IBM is implemented in conjunction with a *physics-compatible* discretization. This is a flourishing class of numerical methods that aim to discretely preserve the underlying mathematical and physical structure of the continuum model. These methods are capable of providing robustness and physical fidelity without the need for artificial stabilization mechanisms, and while keeping the computational cost at affordable levels. In particular, here the attention is focused on discretely enforcing two properties: a) kinetic-energy preservation (KEP), i.e., ensuring that the discretization of the convective term does not spuriously contribute to the discrete kinetic energy balance, and b) pressure-equilibrium preservation (PEP), i.e., the ability of maintaining constant pressure when both pressure and velocity are initially uniform.

This paper presents a description of the proposed approach and a preliminary validation of the method based on a classical aeroacoustic benchmark.

## 2 Numerical formulation

The aeroacoustic problems considered in this work are governed by the compressible Euler equations:

$$\frac{\partial \rho}{\partial t} + \nabla \cdot (\rho \mathbf{u}) = 0, \quad (1a)$$

$$\frac{\partial (\rho \mathbf{u})}{\partial t} + \nabla \cdot (\rho \mathbf{u} \mathbf{u}) = -\nabla P, \quad (1b)$$

$$\frac{\partial (\rho E)}{\partial t} + \nabla \cdot (\rho \mathbf{u} E) = -\nabla \cdot (P \mathbf{u}), \quad (1c)$$

where  $\rho$  is the density,  $\mathbf{u}$  is the velocity vector,  $P$  is the pressure and  $E$  is the specific total energy,  $E = e + 1/2 \|\mathbf{u}\|^2$ , with  $e = RT/(\gamma - 1)$  the specific internal energy,  $R$  the specific gas constant,  $\gamma$  the specific

heat ratio and  $T$  the gas temperature. The system is closed by the ideal-gas equation of state  $P = \rho RT$ . The problem is defined within a simply-connected domain  $\Omega$ , containing *immersed* closed contours  $\mathcal{S}$  that represent solid objects.

### Discretization framework

The conservation equations listed in Eq. (1) are numerically tackled by employing a standard semi-discretization procedure, i.e., they are firstly discretized in space and then integrated in time. Spatial differential operators are treated using centered finite-differencing formulas; all the flow variables are assumed to be co-located in space on a regular Cartesian mesh in the entire domain  $\Omega$ . Time integration is performed using Runge-Kutta methods.

The semi-discretized equations, here shown for simplicity for a one-dimensional case, read:

$$\rho_t = -C_\rho, \quad (2a)$$

$$(\rho u)_t = -C_{\rho u} - \delta_x P, \quad (2b)$$

$$(\rho E)_t = -(C_{\rho e} + C_{\rho k}) - \Pi_{\rho E}, \quad (2c)$$

where subscript  $t$  indicates derivation with respect to time,  $C$  represents the (semi-discretized) convective terms, and  $\delta_x$  is a discrete central-differencing operator. Within this discrete framework, each of the variables in Eqs. (2a)-(2c) is a  $N$ -sized vector, where  $N$  is the number of grid points, and  $\delta_x$  can be represented as a  $N \times N$  derivative matrix.

As stated in Section 1, the discretization aims at enforcing the KEP and PEP properties. The KEP property has been shown to be essential to achieve non-dissipative, stable simulations of compressible discontinuity-free turbulent flows. For compressible flow, a family of KEP, locally-conservative formulations for the convective term has been recently derived by Coppola et al (2019), and can be expressed as

$$C_{\rho\phi}^{\text{KEP}} = \xi \frac{C_{\rho\phi}^D + C_{\rho\phi}^\phi}{2} + (1 - \xi) \frac{C_{\rho\phi}^u + C_{\rho\phi}^\rho}{2}, \quad (3)$$

where  $\phi$  is the transported scalar, e.g.,  $\phi = 1$  for  $C_\rho$  and  $\phi = u$  for  $C_{\rho u}$ , whereas the various  $C$  terms are consistent expansions of the convective terms:

$$C_{\rho\phi}^D = \delta_x \rho u \phi, \quad (4a)$$

$$C_{\rho\phi}^\phi = \phi \delta_x \rho u + \rho u \delta_x \phi, \quad (4b)$$

$$C_{\rho\phi}^u = u \delta_x \rho \phi + \rho \phi \delta_x u, \quad (4c)$$

$$C_{\rho\phi}^\rho = \rho \delta_x u \phi + \phi u \delta_x \rho. \quad (4d)$$

Here  $\xi = 1/2$  is selected, providing the so-called Kennedy-Gruber-Pirozzoli (KGP) formulations, that has proven to be particularly robust in previous studies. When Eq. (3) is used for  $\phi = 1$  and  $\phi = u$ , the resulting algorithm preserves mass, momentum and kinetic energy by convection both globally and locally. Of note, the KGP form admits a convenient and cost-effective finite-volume implementation,

where the numerical flux function (e.g., for a second-order scheme) is computed as  $F_{i+1/2} = 1/8(\rho_i + \rho_{i+1})(u_i + u_{i+1})(\phi_i + \phi_{i+1})$ .

The second component of the novel framework is the enforcement of the PEP condition introduced in Section 1. This property can be easily demonstrated in a continuous setting by considering the one-dimensional velocity- and pressure-evolution equations. For instance, the latter can be derived directly from the internal energy equation exploiting the relationship  $P = \rho e(\gamma - 1)$ , yielding

$$P_t = -\frac{\partial}{\partial x}(Pu) - (\gamma - 1)P \frac{\partial u}{\partial x}. \quad (5)$$

Based on Eq. (5), it can be immediately deduced that when the initial pressure and velocity are spatially constant, i.e.,  $u = \bar{u}$  and  $P = \bar{P}$ , then the pressure does not change in time; it is therefore highly desirable that this equilibrium is discretely preserved also in numerical simulations. In particular, it is hypothesized here that for aeroacoustic simulations with (possibly moving) boundaries, this property can help to further increase the fidelity of the numerical results.

While the KEP property depends exclusively on how the continuity and momentum equations are discretized, the fulfilment of the PEP property depends on the numerical treatment of the energy equation. When the total energy is directly discretized, the pressure equation is an *induced* equation, and whether  $u_t = 0$  and  $P_t = 0$  are satisfied or not has to be verified on a case-by-case basis by deriving the corresponding discrete evolution equations for velocity and pressure. In a pressure-equilibrium framework, i.e., when  $u = \bar{u}$ , it is useful to preliminarily observe that *any* combination of the split forms in Eq. (4) reduces to

$$C_\rho = \bar{u} \delta_x \rho; \quad C_{\rho u} = \bar{u}^2 \delta_x \rho; \quad C_{\rho k} = \frac{\bar{u}^3}{2} \delta_x \rho. \quad (6)$$

The induced discrete equation for velocity reads:

$$u_t = -\frac{1}{\rho} (C_{\rho u} - \bar{u} C_\rho + \delta_x \bar{P}) \quad (7)$$

which, in light of Eq. (6), is easily seen to satisfy  $u_t = 0$  for any choice of the split forms for  $C_\rho$  and  $C_{\rho u}$ .

The induced pressure equation can be obtained from the internal energy one, which is in turn an induced equation and can be obtained by subtracting the (induced) discrete kinetic energy equation to Eq. (2c):

$$\begin{aligned} (\rho e)_t &= (\rho E)_t - \left[ u(\rho u)_t - \frac{u^2}{2} \rho_t \right] = \\ &= - \left[ C_{\rho e} + C_{\rho k} - \left( u C_{\rho u} - \frac{u^2}{2} C_\rho \right) \right] \\ &\quad - [\Pi_{\rho E} - u \delta_x P]. \end{aligned} \quad (8)$$

Taking Eq. (6) into account, and the linear relationship between internal energy and pressure, the induced pressure-evolution equation reads

$$P_t = -(\gamma - 1) [C_{\rho e} + \Pi_{\rho E}]. \quad (9)$$

There are several ways to make sure that  $P_t = 0$  in Eq. (9). Any linear combination of the forms  $C_{pe}^D$  and  $C_{pe}^u$  can be easily shown to be PEP; here, the arithmetic average is selected as in Shima et al (2021) and Singh and Chandrashekar (2021). Furthermore, any discretization of  $\Pi_{\rho E}$  as  $\delta_x P u$ , as its advective expansion, or as their linear combination is also PEP; the choice here is  $\Pi_{\rho E} = P \delta_x u + u \delta_x P$ .

Finally, note that the choice for the term  $C_{\rho k}$  has remained unspecified. Here,  $C_{\rho k} = C_{pe}^{KGP}$ ; however, other choices are possible, notably to enforce consistency in terms of discrete kinetic energy balance, as proposed by Kuya et al (2018). This has not been considered here and could be the subject of future work.

### Immersed boundary method

Boundary conditions on the closed contour(s)  $\mathcal{S}$  are imposed through the IBM. Several classes of immersed boundary methods have been proposed over the last decades – see, e.g., Roy et al (2020) for a recent overview. Generally speaking, the IBM has been historically more developed in the context of incompressible flows, while it has been relatively less explored for compressible flow models. In this work, a so-called *direct-forcing* approach is selected, where boundary conditions on  $\mathcal{S}$  are enforced directly at a discrete level. Similarly as in Seo and Mittal (2011) and De Vanna et al (2020), a ghost-cell approach is employed in the present work. The ghost-cell method provides more flexibility and ease of implementation in terms of imposing both Dirichlet and Neumann conditions, compared to IBM schemes where a forcing term has to be explicitly computed.

The core idea of the ghost-cell IBM is to assign proper values of the flow variables to a certain number of layers of (ghost) points that lie *inside* the contour  $\mathcal{S}$  and close to the boundary, so that the desired boundary condition is (discretely) satisfied on  $\mathcal{S}$ . This is achieved in a sequence of three main steps:

1. The points of  $\Omega$  interior to  $\mathcal{S}$  are identified and tagged, generating two subsets of: i) solid and ii) fluid points. The solid points are further subdivided into ghost points and interior points, see Fig. 1. The number of ghost points (interior points close to  $\mathcal{S}$ ) depends on the order of accuracy of the discretization scheme, and thus on the computational stencil. In this work, three layers of boundary solid points are identified to allow for up to a sixth-order central scheme. For each ghost point, a corresponding *reflected* (image) point is constructed within the fluid domain, based on the local normal vector to the surface, as well as a projection of the point on  $\mathcal{S}$ .
2. The flow variables are interpolated on the reflection (image) points, as well as (if needed) at the projection points on the body. A bilinear interpolation is used as in De Vanna et al (2020), using the four closest surrounding points to each image

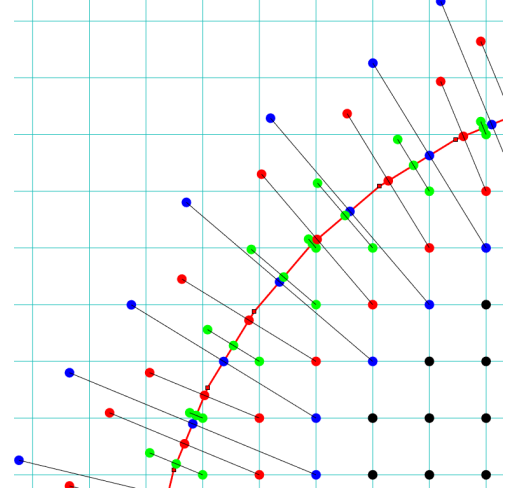


Figure 1: Depiction of the three layers of ghost points, their reflections/projections and the solid interior points. The latter are represented with black dots. The green, red and blue dots contained between the red solid line (geometry) and the interior points represent the three layers of ghost points. The black lines emerging from the ghost points are normal probes that connect them with their projections and reflections, in this sequence. The thin cyan lines represent the Cartesian mesh; their intersections define the computational nodes.

point (in 2D). The primitive variables (velocity, pressure, temperature) are interpolated. Higher-order interpolation kernels, such as those used by Seo and Mittal (2011) were not considered here and might be the subject of future work.

3. Once the primitive variables have been interpolated on the image points, the boundary conditions on  $\mathcal{S}$  are enforced by assigning proper values to the corresponding ghost points. The values depend on the specific nature of boundary condition. For free-slip rigid walls, for instance, the local velocity vector interpolated at the image point  $\tilde{\mathbf{u}}^{\text{ip}}$  is split into a normal and a tangential component,  $\tilde{\mathbf{u}}^{\text{ip}} = \tilde{\mathbf{u}}_{\perp}^{\text{ip}} + \tilde{\mathbf{u}}_{\parallel}^{\text{ip}}$ , and the velocity at the corresponding ghost point is assigned as

$$\mathbf{u} = -\tilde{\mathbf{u}}_{\perp}^{\text{ip}} + \tilde{\mathbf{u}}_{\parallel}^{\text{ip}} \quad (10)$$

General Neumann conditions for a certain variable  $\psi$  are enforced as follows at the ghost points

$$\psi = \psi^{\text{ip}} - \Delta l \left. \frac{\partial \psi}{\partial n} \right|^{\text{p}}, \quad (11)$$

where the last term is the desired normal gradient of the variable at the projection point, on the surface  $\mathcal{S}$ , and  $\Delta l$  is the distance between the ghost point and its image. For steady walls, the homogeneous version of the condition in Eq. (11) is implemented for both pressure and temperature.

Note that the solution is evolved for the entire Eulerian mesh, including the interior points. However, nothing is done for those points; according to the scheme stencil, which at most involves three lateral points, they do not take part in the computation of the fluid region.

### Implementation

The overall methodology has been implemented into a flexible pseudo-spectral solver, where finite-differencing schemes of various order of accuracy are mimicked using the modified wavenumber approach. Nonetheless, the proposed methodology is general, flexible and highly modular and can be easily inserted in any finite-differencing solver.

## 3 Numerical Results

A classical and well-established benchmark is selected to assess the implementation described above: the acoustic wave scattering of a circular cylinder, initially proposed by Tam and Hardin (1997). Despite its simplicity, it has proven to be highly challenging for the accuracy of the underlying numerical method. The test has been performed, among others, by Liu and Vasilyev (2007), Seo and Mittal (2011), Chen et al (2014), Bailoor et al (2017), Brehm et al (2019), Wang et al (2020), in all cases with a certain form of the immersed boundary method, and in conjunction with a large variety of discretization schemes. Furthermore, an analytical solution is available for this problem, as provided by Tam and Hardin (1997).

In the test, a circular cylinder of diameter  $D = 1$  is placed at  $(x, y) = (0, 0)$ , and the pressure is disturbed by a Gaussian pulse at  $(x, y) = (4, 0)$ :

$$p' = \exp\left(-\ln(2)\frac{(x-4)^2 + y^2}{0.2^2}\right). \quad (12)$$

The full non-linear Euler equations are solved on a domain of size  $20 \times 16$  on a uniform Cartesian mesh with different grid sizes  $h$  and central-difference schemes of second, fourth and sixth order of accuracy. Time integration is performed using a standard four-stage Runge-Kutta scheme with  $\Delta t = 0.01$ . Initial conditions include  $\mathbf{u} = 0$ ,  $P = 1/\gamma + p'$  and  $\rho = 1$ . Boundary conditions at the cylinder surface are of free slip for velocity, and homogeneous Neumann for pressure and temperature. At the outer domain, periodic boundary conditions are imposed; the domain is selected to be sufficiently large so that the pressure disturbance does not reach the domain boundary within the simulated time. In addition to simplify the implementation in a pseudo-spectral code, this choice completely eliminates the influence of boundary conditions.

Figure 2 reports the time evolution of the pressure disturbance  $p' = P - 1/\gamma$  at the point  $(x, y) = (2, 0)$ , which is in between the initial location of the pulse and the cylinder. The plot shows the passage of the initial pulse ( $t \approx 2$ ) and the first reflected wave front ( $t \approx 5$ ); also, two parts of the principal wave front split by the cylinder traverse its span, collide, and merge,

thereby generating a third acoustic wave front ( $t \approx 8$ ), as reported by Liu and Vasilyev (2007). The influence of the scheme order for  $h = D/40$ —as previously used by Wang et al (2020) and Chen et al (2014), among others—is shown in Figure 2(left). The second-order scheme displays significant dispersion errors already at the passage of the first pulse, confirming its well-known inability to solve delicate wave propagation problems such as the one under study; the errors are mitigated as the order of accuracy is increased. On the other hand, Figure 2 shows results for the sixth-order accurate scheme at three different resolutions,  $h = D/20$ ,  $h = D/25$  and  $h = D/40$ . Results are in good agreement with the analytical solution, although some waves of small amplitude can be observed even at the finest spatial resolution. The waves are produced after the impact of the acoustic pulse with the cylinder, and are therefore attributed to the immersed-boundary formulation utilized in this work.

Contours of the pressure disturbance  $p' = P - 1/\gamma$  are shown in Figure 3 at four different times, depicting the initial transport of the pulse, its reflection, and later stages of the complex wave pattern that emerges from this configuration. Results refer to the sixth-order scheme at a resolution  $h = D/40$ . The wave propagation is generally well captured and in line with previous work, e.g., Bailoor et al (2017) and Seo and Mittal (2011), not shown here. Some spurious wiggles are visible in the wave pattern reflected from the cylinder, as discussed above, and require further investigation in terms of the interpolation accuracy of the IBM.

Finally, the behaviour of the method is also assessed with regards to the reflected wave at a probe located at  $(x, y) = (0, 5)$ . Results are shown in Figure 4, and compared to both analytical and literature references. The current method is reported for the sixth-order accurate scheme and  $h = D/40$ . Of note, literature results were all obtained at this same spatial resolution. The current method correctly captures the phase of the wave, while only slightly underestimating its amplitude. It performs very well compared to the other schemes; note that Sun et al (2012) used a fourth-order dispersion-relation preserving scheme, while Chen et al (2014) employed a Lattice-Boltzmann method. Interestingly, the spurious wave generated at the interface and previously mentioned appear to have disappeared at this location, and/or not to affect this part of the domain.

## 4 Discussion and conclusions

The broad, long-term objective of this research is to contribute to the implementation of high-fidelity CFD in complex scenarios of practical interest. In this regard, a robust, efficient and accurate methodology for direct computation of sound generated by multi-scale (e.g., turbulent) flow sources is being developed. The proposed approach combines the immersed boundary method with a discretization framework that preserves important non-linear properties

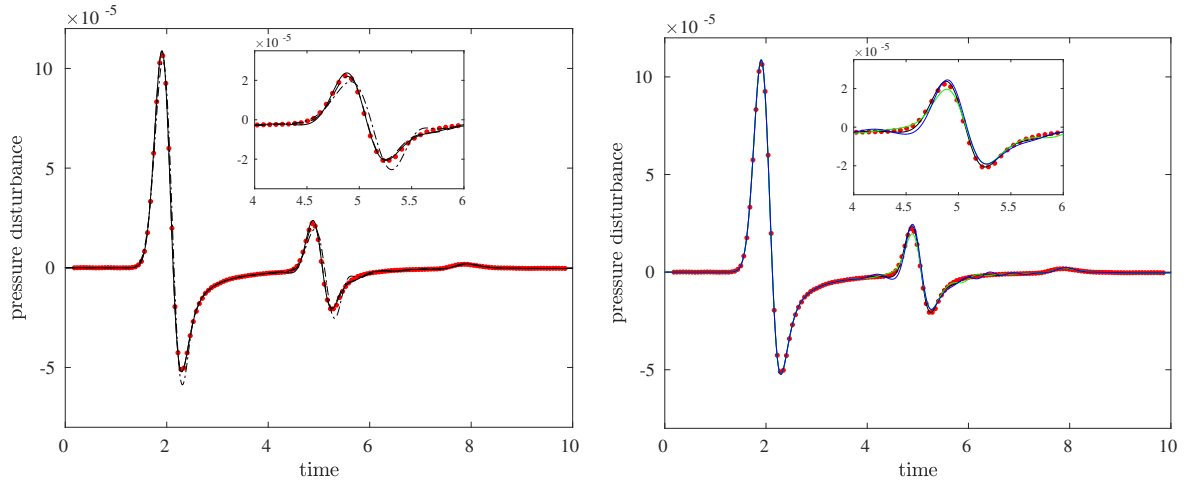


Figure 2: Time evolution of the pressure perturbation  $p' = P - 1/\gamma$  at the point  $(x, y) = (2, 0)$ . The inset plot shows a zoom for  $t \in [4, 6]$ . Left: second-order (dash-dotted line); fourth-order (dotted) and sixth-order (solid) schemes at  $h = D/40$ . Right: sixth-order scheme at  $h = D/20$  (blue),  $h = D/25$  (green) and  $h = D/40$  (black). Red circles: analytical solution.

of the continuous model, such as kinetic-energy and pressure-equilibrium preservation.

In this work, the method was described and preliminarily validated in terms of acoustic scattering of a circular cylinder. Although this test is mostly concerned with linear wave propagation, it allowed to identify certain ingredients of the algorithm that need further improvement; most importantly, a bilinear interpolation at the IB interface appears to be unsuitable in conjunction with a higher-order central scheme, as it produced small (but non-negligible) spurious waves. Further work is underway to overcome this limitation; the optimization of the underlying scheme in terms of linear dissipation/dispersion properties, as classically done in CAA, also warrants examination.

## Acknowledgments

This work is supported by the *Industrial Doctorate* programme (2022-DI-040) of the *Generalitat de Catalunya* (Catalonia), the *Beatriz Galindo* programme (Distinguished Researcher, BGP18/00026) of the *Ministerio de Ciencia, Innovación y Universidades* (Spain), and the *Serra Hùnter* programme (Catalonia).

## References

- Bailoor, S., Annangi, A., Seo, J. H. and Bhardwaj, R. (2017), Fluid–structure interaction solver for compressible flows with applications to blast loading on thin elastic structures, *Appl. Math. Model.*, Vol. 52, pp. 470–492.
- Roy, S., De, A. and Balaras, E. (2020), *Immersed Boundary Method*, Springer Singapore.
- Brehm, C., Barad, M. F. and Kiris, C. C. (2019), Development of immersed boundary computational aeroacoustic prediction capabilities for open-rotor noise, *J. Comp. Phys.*, Vol. 388, pp. 690–716.
- Capuano, F., Coppola, G., Rández, L. and de Luca, L.

(2017), Explicit Runge–Kutta schemes for incompressible flow with improved energy-conservation properties, *J. Comput. Phys.*, Vol. 328, pp. 86–94.

Chen, L., Yu, Y., Lu, J. and Hou, G. (2014), A comparative study of lattice Boltzmann methods using bounce-back schemes and immersed boundary ones for flow acoustic problems, *Int. J. Numer. Methods Fluids*, Vol. 74(6), pp. 439–467.

Colonus, T. and Lele, S. K. (2004), Computational aeroacoustics: progress on nonlinear problems of sound generation, *Prog. Aerosp. Sci.*, Vol. 40(6), pp. 345–416.

Coppola, G., Capuano, F., Pirozzoli, S. and de Luca, L. (2019), Numerically stable formulations of convective terms for turbulent compressible flows, *J. Comput. Phys.*, Vol. 382, pp. 86–104.

De Vanna, F., Picano, F. and Benini, E. (2020), A sharp-interface immersed boundary method for moving objects in compressible viscous flows, *Comput. Fluids*, Vol. 201, p. 104415.

Kuya, Y., Totani, K. and Kawai, S. (2018), Kinetic energy and entropy preserving schemes for compressible flows by split convective forms, *J. Comput. Phys.*, Vol. 375, pp. 823–853.

Liu, Q. and Vasilyev, O. V. (2007), A Brinkman penalization method for compressible flows in complex geometries, *J. Comput. Phys.*, Vol. 227(2), pp. 946–966.

Seo, J. H. and Mittal, R. (2011), A high-order immersed boundary method for acoustic wave scattering and low-Mach number flow-induced sound in complex geometries, *J. Comput. Phys.*, Vol. 230(4), pp. 1000–1019.

Shima, N., Kuya, Y., Tamaki, Y. and Kawai, S. (2021), Preventing spurious pressure oscillations in split convective form discretization for compressible flows, *J. Comput. Phys.*, Vol. 427, p. 110060.

Singh, V. and Chandrashekar, P. (2021), On a linear stability

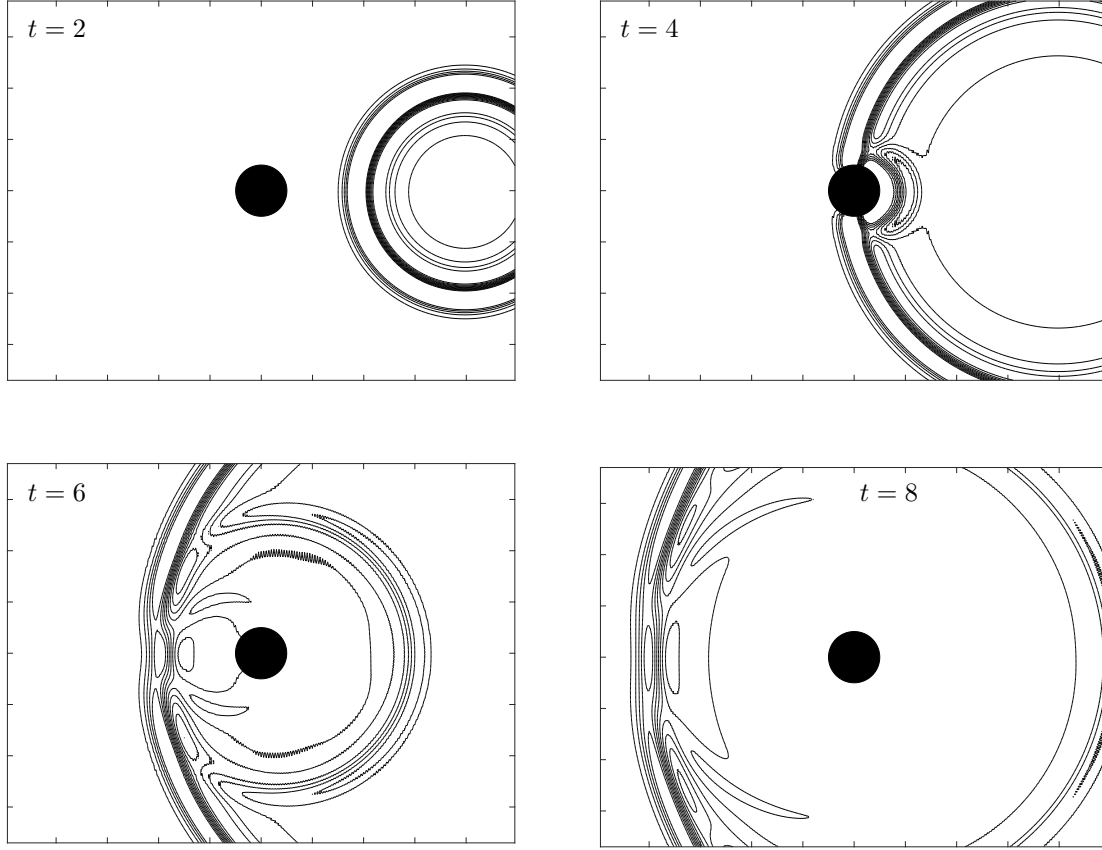


Figure 3: Contours of the pressure perturbation  $p' = P - 1/\gamma$  at four different times (10 contour levels between  $-4e-5$  and  $4e-5$ ). Results were obtained with a 6th-order central scheme and a spatial resolution  $\Delta x = \Delta y = 0.025 = D/40$ .

issue of split form schemes for compressible flows. *arXiv preprint*, arXiv:2104.14941.

Sun, X., Jiang, Y., Liang, A. and Jing, X. (2012), An immersed boundary computational model for acoustic scattering problems with complex geometries, *J. Acoust. Soc. Am.*, Vol. 132(5), pp. 3190–3199.

Tam, C. K. W. and Hardin, J. C. (1997), Second Computational Aeroacoustics (CAA) Workshop on Benchmark Problems, NASA-CP-3352.

Verzicco, R. (2023), Immersed boundary methods: Historical perspective and future outlook, *Annu. Rev. Fluid Mech.*, Vol. 55, pp. 129–155.

Wang, L., Tian, F. B. and Lai, J. C. (2020), An immersed boundary method for fluid–structure–acoustics interactions involving large deformations and complex geometries, *J. Fluids Struct.*, Vol. 95, p. 102993.

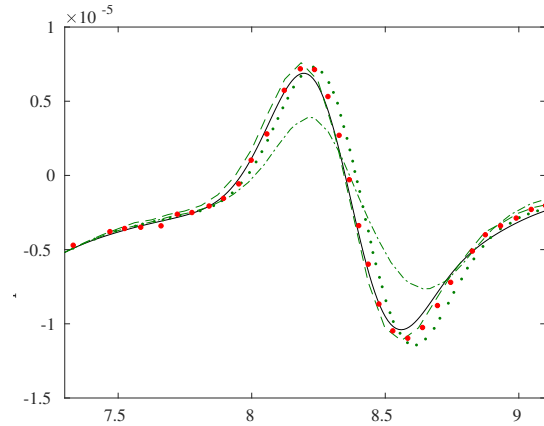


Figure 4: Time evolution of the pressure perturbation  $p' = P - 1/\gamma$  at point  $(x, y) = (0, 5)$ . Shown are results from: present method with sixth-order scheme and  $h = D/40$  (black solid line); Wang et al (2020) (dotted); Sun et al (2012) (dashed); explicit method by Chen et al (2014) (dash-dotted). Red circles: analytical solution.